



## OPEN ACCESS

## EDITED BY

Myriam Roussigne,  
CNRS/Toulouse University  
UMR5077louse, France

## REVIEWED BY

Jeffrey Amack,  
Upstate Medical University, United States  
Hiroshi Hamada,  
RIKEN Center for Biosystems Dynamics  
Research (BDR), Japan  
Martin Blum,  
University of Hohenheim, Germany

## \*CORRESPONDENCE

Paul A. Trainor,  
✉ pat@stowers.org

## SPECIALTY SECTION

This article was submitted to  
Morphogenesis and Patterning,  
a section of the journal  
Frontiers in Cell and  
Developmental Biology

RECEIVED 26 December 2022

ACCEPTED 23 February 2023

PUBLISHED 11 April 2023

## CITATION

Shylo NA, Smith SE, Price AJ, Guo F,  
McClain M and Trainor PA (2023),  
Morphological changes and two *Nodal*  
paralogs drive left-right asymmetry in the  
squamate veiled chameleon  
(*C. calyptratus*).  
*Front. Cell Dev. Biol.* 11:1132166.  
doi: 10.3389/fcell.2023.1132166

## COPYRIGHT

© 2023 Shylo, Smith, Price, Guo, McClain  
and Trainor. This is an open-access article  
distributed under the terms of the  
[Creative Commons Attribution License  
\(CC BY\)](https://creativecommons.org/licenses/by/4.0/). The use, distribution or  
reproduction in other forums is  
permitted, provided the original author(s)  
and the copyright owner(s) are credited  
and that the original publication in this  
journal is cited, in accordance with  
accepted academic practice. No use,  
distribution or reproduction is permitted  
which does not comply with these terms.

# Morphological changes and two *Nodal* paralogs drive left-right asymmetry in the squamate veiled chameleon (*C. calyptratus*)

Natalia A. Shylo<sup>1</sup>, Sarah E. Smith<sup>1</sup>, Andrew J. Price<sup>1</sup>, Fengli Guo<sup>1</sup>,  
Melainia McClain<sup>1</sup> and Paul A. Trainor<sup>1,2\*</sup>

<sup>1</sup>Stowers Institute for Medical Research, Kansas City, MO, United States, <sup>2</sup>Department of Anatomy and Cell Biology, University of Kansas Medical Center, Kansas City, MO, United States

The ancestral mode of left-right (L-R) patterning involves cilia in the L-R organizer. However, the mechanisms regulating L-R patterning in non-avian reptiles remains an enigma, since most squamate embryos are undergoing organogenesis at oviposition. In contrast, veiled chameleon (*Chamaeleo calyptratus*) embryos are pre-gastrula at oviposition, making them an excellent organism for studying L-R patterning evolution. Here we show that veiled chameleon embryos lack motile cilia at the time of L-R asymmetry establishment. Thus, the loss of motile cilia in the L-R organizers is a synapomorphy of all reptiles. Furthermore, in contrast to avians, geckos and turtles, which have one *Nodal* gene, veiled chameleon exhibits expression of two paralogs of *Nodal* in the left lateral plate mesoderm, albeit in non-identical patterns. Using live imaging, we observed asymmetric morphological changes that precede, and likely trigger, asymmetric expression of the *Nodal* cascade. Thus, veiled chameleons are a new and unique model for studying the evolution of L-R patterning.

## KEYWORDS

left-right patterning, left-right organizer, gastrulation, cilia, cell migration, *Nodal*, lefty, veiled chameleon

## Introduction

Asymmetries are deeply rooted in the phylogenetic tree and are frequently driven by the ancient *Nodal* signaling cascade. For example, *Nodal* drives the asymmetric positioning of asexual buds in radially symmetric hydra (Watanabe et al., 2014). A duplication event resulted in two *Nodal* genes in gnathostomes, with additional expansion events in fish and frogs (Opazo et al., 2019). In contrast, mammals and avians retained a single copy of *Nodal* each, but different paralogs (Opazo et al., 2019; Kajikawa et al., 2020). Henceforth we will refer to mammalian *Nodal* as *Nodal1*, and to avian *Nodal* as *Nodal2*, after Kajikawa et al., (2020). The *Nodal* molecular cascade drives the establishment of left-right (L-R) asymmetry in deuterostomes, but what initiates asymmetric *Nodal* expression across phyla remains poorly understood. This is in part due to the constraints of the limited model organisms utilized.

A L-R organizer (LRO) is a transient organ or organizing region in deuterostomes, and motile cilia and asymmetric cilia-generated flow have been shown to be a synapomorphy of deuterostome LROs, from sea urchins to humans (Blum and Ott, 2018). Interestingly, avians, as well as some even-toed ungulates (Gros et al., 2009) lack motile cilia in their LROs.

Instead, asymmetric *Nodal* expression and L-R asymmetry are established through asymmetric cell movements and tilting of the LRO, which are tightly linked to primitive streak formation (Cui et al., 2009; Gros et al., 2009). What triggers this asymmetric tissue morphogenesis currently remains unknown.

Non-avian reptiles comprise 40% of all living amniotes, yet their early development remains poorly understood. One of the major challenges is accessing early-stage reptilian embryos for detailed analysis. Access is often restricted to short breeding seasons, and further complicated by the fact that most squamate embryos are undergoing organogenesis at the time of oviposition, thus necessitating euthanasia of the mother for the study of L-R patterning events (Diaz et al., 2015a; Diaz et al., 2017). Thus, it was only recently revealed that turtles and geckos, like avian reptiles, lack motile cilia in their LRO (Kajikawa et al., 2020). However, unlike avians, no L-R asymmetric tissue morphogenesis was noted (Kajikawa et al., 2020). Furthermore, each retained only *Nodal2* in their genomes, suggesting that loss of motile cilia in the LRO and loss of *Nodal1* may be synapomorphies of all reptiles (Kajikawa et al., 2020).

Veiled chameleons (*Chamaeleo calyptratus*) breed year-round, depositing large clutches of eggs (Diaz et al., 2015b). Most importantly, veiled chameleon embryos are pre-gastrula at oviposition, making them an excellent research organism for studying the mechanisms governing the regulation and evolution of gastrulation and L-R patterning (Diaz et al., 2019). We discovered that in contrast to other reptiles described to-date, veiled chameleon embryos express both *Nodal1* and *Nodal2* in a L-R asymmetric manner. Furthermore, we found that veiled chameleons lack motile cilia in their LRO region. Therefore, we used live imaging to track the timing and pattern of asymmetric tissue rearrangements to provide a deeper understanding of gastrulation and the establishment of L-R asymmetry in squamates. We find that asymmetric morphological changes occur prior to the onset of molecular L-R asymmetry. The tissue rearrangements that we observed differ from chicken and even-toed ungulate embryos, since non-avian reptiles lack a primitive streak, and instead use a blastopore and involution for gastrulation. Thus, veiled chameleons can serve as a new model for studying the evolution of gastrulation and L-R patterning.

## Results

### Left-right patterning features in veiled chameleons

Embryonic turning is a distinct developmental event in the establishment of asymmetry during amniote embryogenesis. Previously it was assumed in chicken embryos, that asymmetric heart looping drove asymmetric embryo turning (Waddington, 1937). However, these processes can be de-coupled and are considered distinct independent developmental events (Hoyle et al., 1992; Levin et al., 1997). In veiled chameleon, embryo turning initiates with the head turning to the right at around the 4-somite stage (4ss) (Figures 2G, N, V), prior to the formation of the heart tube and subsequent heart looping. MF-20 staining reveals the formation of two heart fields at the 5-6ss (Figure 1A), which then fuse into a heart tube, that forms at an angle, pre-positioned for

subsequent heart looping (Figure 1B). A heartbeat typically becomes detectable by the 10ss, concomitant with the heart undergoing looping morphogenesis (Figures 1C–E), resulting in a three-chambered organ (Figure 1F).

The heart is positioned high in the chest and is one of many structurally and positionally asymmetrical organs (Figure 1G). Veiled chameleon lungs have single 3-chambered lobes on each side (Figure 1H). Both lungs have structures of unknown function, unique to chameleons, called diverticula (Klaver, 1973). The left lung has a single row of five diverticula, whereas the right lung has two rows of three and four diverticula (Figure 1H). The left lung is notably shorter than the right lung. The liver has a larger lobe on the right side, similar to other animals (Figure 1I). The urogenital system is asymmetric in both sexes, with the axial position of the gonads and kidneys on the right being slightly more anterior than on the left (Figures 1J, K). The gastrointestinal system is relatively short, with the stomach positioned on the left side, and a single characteristic loop of the intestine projecting towards the right side of the body (Figures 1G, L).

### *Nodal1* and *Nodal2* are both present in veiled chameleon transcriptome and are expressed asymmetrically during L-R patterning

Although a transcriptome of limited size was already available for veiled chameleons, it poorly correlated with the stages of development examined in this study (Pinto et al., 2019). Therefore, we collected a pool of embryos from St. 7 to 8 somites (Supplementary Dataset S1) and carried out Iso-seq (PacBio) to assemble a new transcriptome, which revealed the presence of most genes in the *Nodal* pathway and thus their expression during gastrulation and early somitogenesis stages. Notably, we identified two different transcripts for *Nodal*. Evolutionary comparison between predicted open reading frames and proteins from other animals revealed one of the transcripts as *Nodal*, and the other transcript as being *Nodal-like*. We adapted the nomenclature proposed by Kajikawa et al., (2020), and henceforth will refer to the former as *Nodal1* and the latter as *Nodal2* (Kajikawa et al., 2020) (Supplementary Figure S1). Thus, contrary to a previous report that *Nodal1* was lost in reptiles (Kajikawa et al., 2020), we discovered that *Nodal1* was retained in veiled chameleons. Furthermore, subsequent genomic and phylogenetic analyses revealed several other squamate species have also retained *Nodal1* in their genomes (Supplementary Figure S1).

We next examined the expression pattern of *Nodal1* and *Nodal2* at the time of L-R establishment to infer their roles in this process (Figure 2). Both *Nodal* transcripts exhibit a dynamic pattern of expression that suggests involvement in both gastrulation and L-R patterning. *Nodal1* and *Nodal2* are expressed symmetrically during gastrulation at stages 7-7+ in the blastopore (Figures 2A, B, H, I). In both cases, expression is in the chordamesoderm in the anterior region (Figures 2A', H') and in the chordamesoderm and blastopore plate more posteriorly (Figures 2A'', I') (Gilland et al., 2004). The differences in expression pattern are suggestive of distinct functions in gastrulation. With the onset of neurulation at stage 8 and appearance of the prechordal plate (Supplementary Dataset

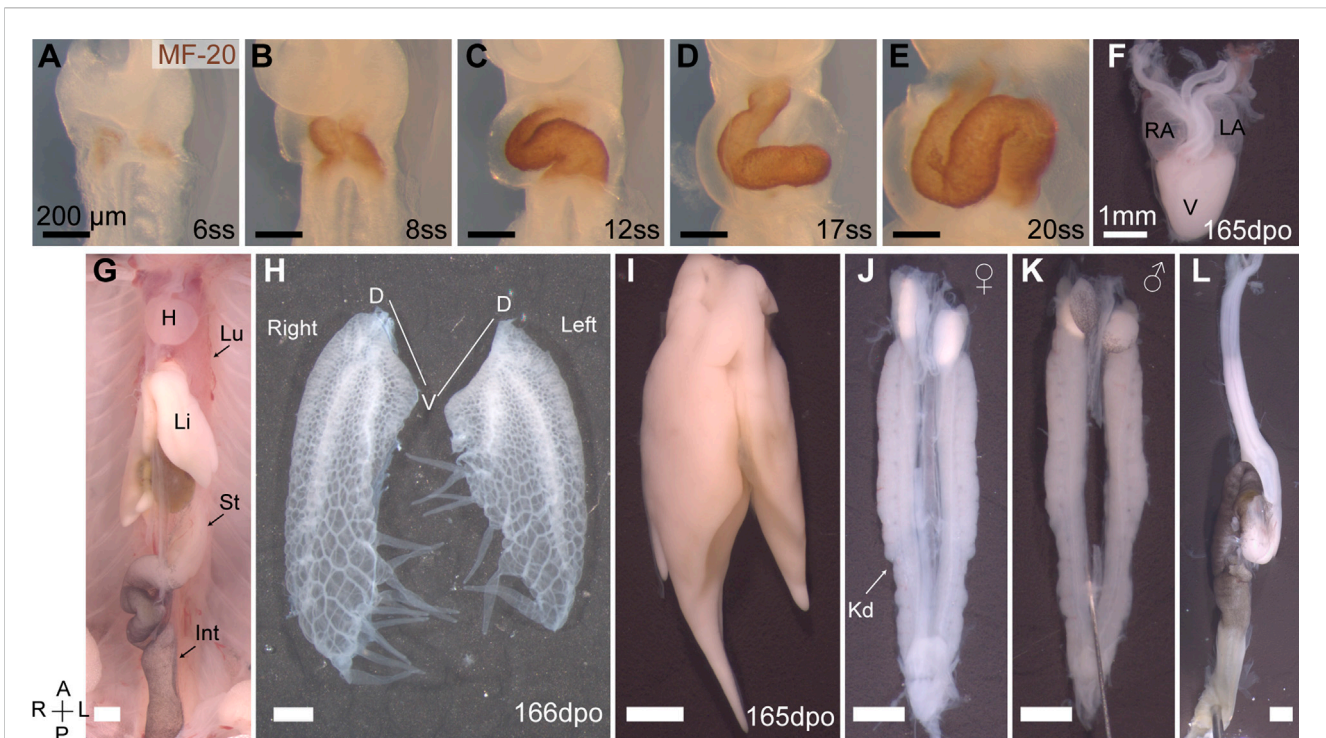


**FIGURE 1**

Organ asymmetry in veiled chameleon embryos. (A–F) Progression of heart formation and development. In (A–E) the formation of the heart is highlighted through immunohistochemical staining for MF-20. (F) The heart of pre-hatching stage embryos (165 dpo—days post oviposition) has three chambers—left and right atria (LA and RA, respectively) and one ventricle (V). (G) General overview of abdominal organs in 165 dpo embryo. Heart (H), lungs (Lu), liver (Li), stomach (St), intestine (Int) are labeled. (H) Lungs of a 166 dpo embryo have a single 3-chambered lobe on each side. The left lung is shorter than the right. Chameleons have unique diverticula on ventral ends of the lungs on both sides. Diverticula are arranged in two rows on the right lung, and in a single row on the left lung. The left lung has 5, and the right has 3 + 4 diverticula. (I) The liver has a larger lobe on the right side. (J, K) The urogenital system of both females (J) and males (K) exhibits L-R asymmetry with the left gonad being lower than the right. Kidneys (Kd) are elongated and lie flat against the dorsal abdominal wall. (L) The gastrointestinal tract is relatively short, with stomach on the left side. The intestine posterior to the stomach has a single major loop and have black pigmentation. All panels show ventral view, unless otherwise noted. Anterior (A) is on the top, posterior (P) is on the bottom, left (L) is on the reader's right, and right (R) is on the reader's left. All black scale bars are 200 µm, all white scale bars are 1mm.

S1), the expression of both transcripts is extinguished, and remains absent through the early stages of the midline, head process and foregut formation (Figures 2C, D, J, K). *Nodal2* expression re-emerges just prior to the initiation of somitogenesis in a narrow domain just anterior to the blastopore slit in the left presomitic mesoderm (Figures 2L, L'). In a stage-matched embryo, *Nodal1* remains switched off (Figure 2E). With the onset of somitogenesis, *Nodal2* expression propagates to the left lateral plate mesoderm (LPM) in the posterior end of the embryo (Figures 2M, M'). Whether in response to *Nodal2*, or independent of *Nodal2*, *Nodal1* likewise becomes expressed in the LPM, in a much more diffuse manner (Figures 2F, F'). The expression of both *Nodal1* and *Nodal2* then expands in the left LPM but is downregulated and switched off by the 4ss (Figures 2G, N).

Smad2 becomes phosphorylated as the result of Nodal activity. For ease of analysis, we normalized pSmad2 expression against DAPI staining (Supplementary Figures S3I–P) and carried out an intensity analysis to compare left and right sides (Supplementary Figures S3I'–P'). We do not observe specific enrichment of pSmad2 near the blastopore during the late stages of gastrulation, suggesting that *Nodal1/2* molecules may act through a different pathway at this stage (Figures 2O–S; Supplementary Figures S3I–M,

I'–M'). With the onset of somitogenesis, broad pSmad2 expression becomes apparent in the left LPM, and lingers until the 4ss, slightly later than the expression of *Nodal1/2* (Figures 2T–V; Supplementary Figures S3N–P, N'–P'). Notably, we did not observe an enrichment of pSmad2 in the presomitic mesoderm, in contrast to a previous report about the Madagascar ground gecko (Kajikawa et al., 2020).

## The expression patterns of key members of the Nodal cascade align with *Nodal1/2* expression

Characterizing the dynamic expression of *Nodal1* and *Nodal2* and their activity allowed us to narrow down the timing of L-R patterning events in veiled chameleons. We then set out to identify and examine the expression patterns of other genes in the Nodal cascade. We identified a single *Lefty* gene in veiled chameleons as is typical for most vertebrates (Hashimoto et al., 2007). *Lefty* is a well-known repressor of *Nodal*. In chicken and mouse embryos, *Lefty* is expressed in the LPM and the midline, acting both as a midline barrier, and repressor of *Nodal* in the LPM through an activator-inhibitor loop (Nakamura et al., 2006). Prior studies have suggested that midline *Lefty* expression is more critical for *Nodal* inhibition



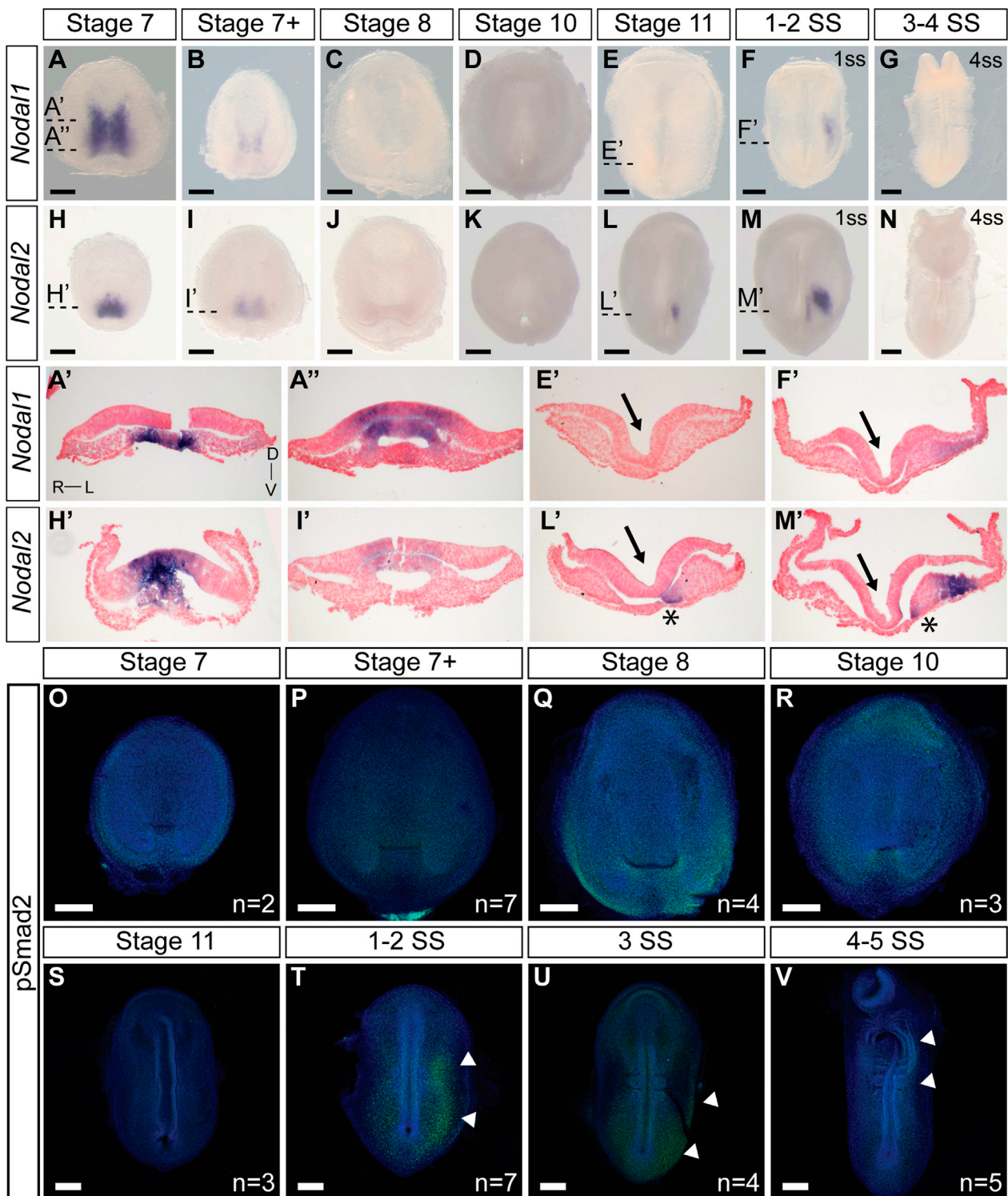


**FIGURE 2**

Expression and activity of *Nodal1* and *Nodal2* in veiled chameleon embryos. All embryos are presented in ventral view, unless otherwise noted. Dorsal view available in [Supplementary Figures S2, S3](#). (A–G) Whole mount RNA *in situ* hybridization for *Nodal1* expression. (H–N) Whole mount RNA *in situ* hybridization for *Nodal2* expression. (A', A'', E', F', H', I', L', M') Transverse sections of embryos from (A–N), as indicated with dashed lines. Sections were counterstained with nuclear fast red for better visualization. Section orientation is as indicated in (A'). Asterisk denotes *Nodal2* expression in presomitic mesoderm. Arrows point to the medial hinge point of the neural tube. (O–V) The presence of active Nodal signaling was evaluated through antibody staining for pSmad2 (green), with nuclear Dapi staining in blue. White arrowheads denote areas of pSmad2 enrichment visible in this view. Normalized pSmad2 staining of embryos and intensity analysis between left and right sides is available in [Supplementary Figure S3](#). n indicates the number of embryos examined for a given stage. All scale bars are 200  $\mu$ m.

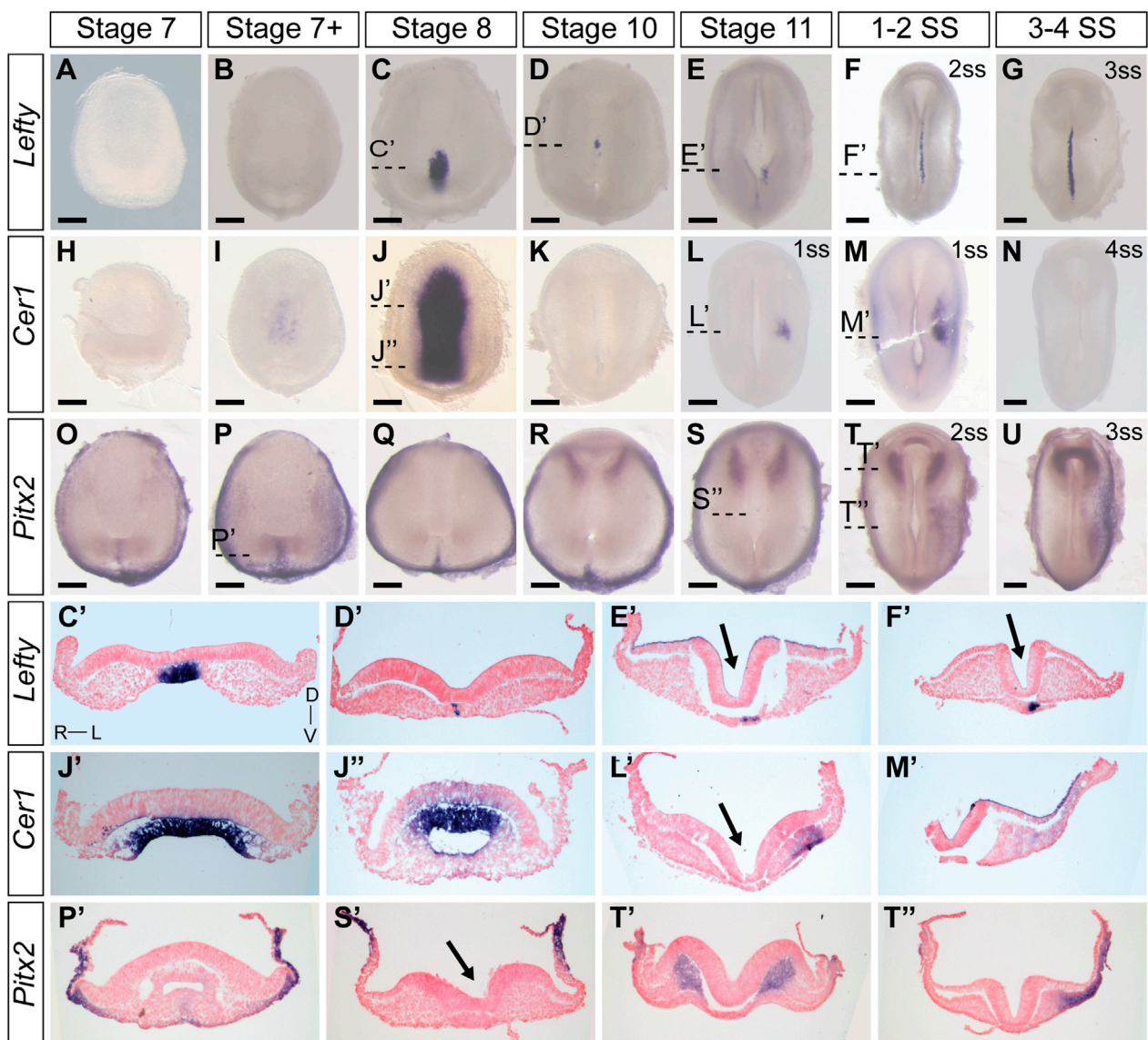


**FIGURE 3**

Expression patterns of key members of the Nodal cascade in veiled chameleon embryos. All embryos are presented in ventral view, unless otherwise noted. Dorsal view available in [Supplementary Figure S4](#). (A–G) Whole mount RNA *in situ* hybridization for *Lefty* expression. (H–N) Whole mount RNA *in situ* hybridization for *Cer1* expression (O–U). Whole mount RNA *in situ* hybridization for *Pitx2* expression. (C', D', E', F', J', J'', I', M', P', S', T', T'') Transverse sections of embryos from (A–U), as indicated with dashed lines. Sections were counterstained with nuclear fast red for better visualization. Section orientation is as indicated in (C'). Arrows point to the medial hinge point of the neural tube. All scale bars are 200  $\mu$ m.

than its LPM expression, and under certain conditions *Lefty* expression may be downregulated without disrupting the signaling cascade (Nakamura et al., 2006; Rogers et al., 2017). *Lefty* expression in veiled chameleon embryos provides *in vivo* evidence for this model. In veiled chameleons *Lefty* is expressed exclusively in the midline (Figures 3A–G). It has strong symmetrical expression in the notochordal plate at stage 8, as *Nodal* becomes downregulated (Figures 3C, C'). The symmetrical midline expression of *Lefty* then becomes extinguished (Figures 3D, D'), followed shortly by its re-expression exclusively in the left side of the notochordal plate, which is distinct from its expression in left side of the floor plate of mouse and chicken embryos (Meno et al., 1998; Rodriguez Esteban et al., 1999) (Figures 3E, E'). *Lefty* is initially

expressed just anterior to the blastopore, at the axial level of early *Nodal2* expression, and then propagates anteriorly through the entire length of the notochordal plate, before being switched off by 4–5ss (Figures 2L, 3E, E', F, F', G and not shown). The lack of *Lefty* expression in the LPM, therefore leaves the system without an off switch for *Nodal1/2* expression in the LPM.

*Dand5*(*Cer12/Coco/Charon*) is the first asymmetrically expressed member of the Nodal cascade and acts to regulate the repression of *Nodal* (Maerker et al., 2021). Interestingly, we found no evidence for *Dand5* expression in the veiled chameleon transcriptome, and it appears to have been lost in all reptilian clades (Kajikawa et al., 2020). Since *Cer1* acts as the asymmetric repressor of *Nodal2* in chicken embryos, and belongs to the same



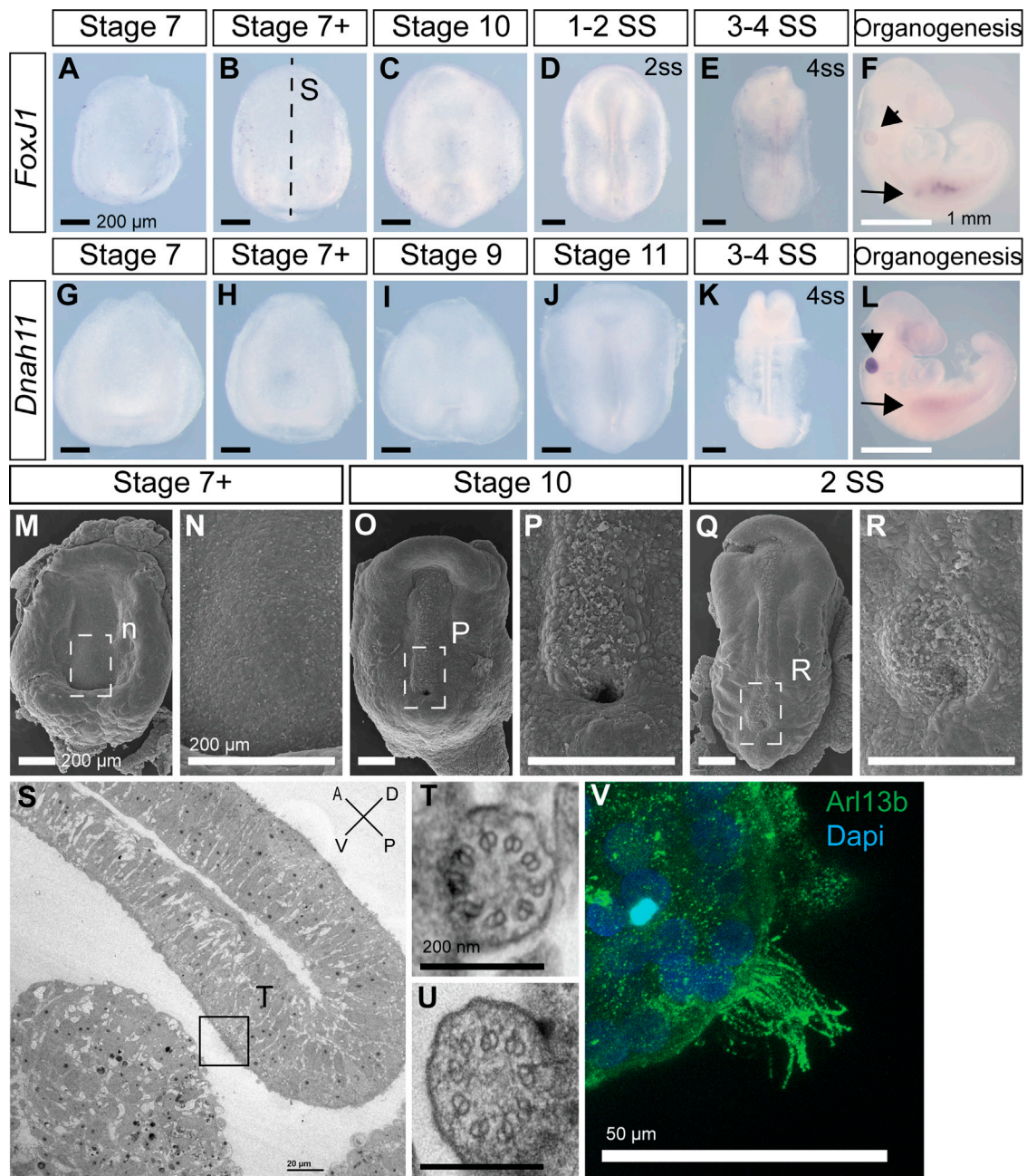


**FIGURE 4**

Veiled chameleon embryos lack motile cilia during L-R asymmetry establishment. All embryos are presented in ventral view, unless otherwise noted. Dorsal view available in [Supplementary Figure S5](#), where possible. (A–F) Whole mount RNA *in situ* hybridization for *FoxJ1* expression. (G–L) Whole mount RNA *in situ* hybridization for *Dnah11* expression. (F, L) Arrowheads indicate gene expression in otic vesicle, arrows indicate gene expression in the kidney—both areas known to have motile cilia. Black scale bars in (A–E, G–K) are 200  $\mu$ m. White scale bars in (F, L) are 1 mm. (M–R) SEM visualization of embryos. Dashed rectangular areas in (M, O, Q) are enlarged in (N, P, R). All scale bars in (M–R) are 200  $\mu$ m. (S–U) TEM images. (S) Sagittal section through an embryo, as indicated with a dashed line in B for a stage-matched embryo. Embryo orientation is as indicated, with blastoporal lip located dorsally. Scale bar 20  $\mu$ m. Boxed region indicates exact location of the cilium, depicted in T. (T, U). Cross sections of two cilia, located near the blastopore, as indicated in S. Both cilia have 9 + 0 structure and lack axonemal dyneins, pointing to their nature as primary, non-motile cilia. Scale bars are 200 nm. (V) Fluorescent immunostaining of motile multicilia in dissociated kidney cells. Ciliary marker Arl13b is in green, nuclei labeled with Dapi in blue. Video of ciliary movement is available in [Supplementary Video S1](#). Scale bar is 50  $\mu$ m.

family as *Dand5*, we focused on the pattern of *Cer1* expression instead (Rodríguez Esteban et al., 1999; Belo et al., 2009). *Cer1* is not expressed in veiled chameleon embryos at stages 7 and 7+, prior to stage 8; and the lack of expression in the head region suggests it might play a lesser role in the anterior visceral endoderm than in

other species (Belo et al., 2009). However, we observed a huge, but temporary burst of *Cer1* in the chordamesoderm at stage 8 that coincides with downregulation of both *Nodal* genes (Figures 2C, J, 3J, J', J'', K). *Cer1* is re-expressed later in the LPM, in a pattern reminiscent of *Nodal1* expression (Figures 2F, F', 3L, L', M, M').

*Cer1* expression is then downregulated by the 4-somite stage, similar to *Nodal1/2*. Overall, the dynamic pattern of *Cer1* expression is consistent with it being induced by *Nodal*, and then acting as a strong repressor of *Nodal1/2*, similar to its activity in chicken embryos (Tavares et al., 2007).

*Pitx2* serves as a critical transcriptional regulator of L-R asymmetry in vertebrates (Ryan et al., 1998; Yoshioka et al., 1998; Lin et al., 1999) and we observed that *Pitx2* is expressed broadly in gastrulating veiled chameleon embryos (Figures 3O–R, P'). Subsequently, *Pitx2* expression becomes mostly restricted to the head mesoderm, as in other animals (Ryan et al., 1998) (Figures 3R, S, T, T', U), and the left LPM (Figures 3T, T'', U). Thus, the core of the Nodal signaling cascade is conserved in veiled chameleons, and the observed changes provide a framework to understand the mechanics of the process, as well as the opportunity for comparative analyses of gene and protein function evolution.

## Veiled chameleon lacks motile cilia at the left-right organizer

Most deuterostomes examined to-date, ranging from sea urchins to humans, use motile cilia in the LRO to establish L-R asymmetry (Blum et al., 2009; Blum et al., 2014). Transcription factor *Foxj1* induces the formation of motile cilia, and its loss leads to L-R patterning defects (Chen et al., 1998). *Dnah11* is an axonemal dynein, required for ciliary motility, and is mutated in the classical L-R patterning mouse mutant *inversus viscerum* (*iv*) (Supp et al., 1997). Interestingly, we could not detect expression of *Foxj1* and *Dnah11* in veiled chameleons during the establishment of L-R patterning (Figure 4A–E, G–K). Both *Foxj1* and *Dnah11* are however expressed at later stages of veiled chameleon development, most notably in the otic vesicle (arrowheads in Figures 4F, L), and kidneys (arrows in Figures 4F, L). The kidneys of many animals are known to contain motile cilia (Marra et al., 2016), and we confirmed the presence of motile cilia in veiled chameleon kidneys through direct imaging of dissociated cells from the kidneys (Figure 4V; Supplementary Video S1). We also verified our findings by performing SEM and TEM analyses of Stage 7+, 10 and 2ss veiled chameleon embryos especially near the blastopore, the presumed LRO (Kajikawa et al., 2020). We found no evidence of motile-like cilia via SEM but observed short primary cilia throughout the embryos (Figures 4M–R). We carried out TEM analysis in two Stage 7 + embryos and identified 22 cilia with 9 + 0 microtubule arrangement, spread out throughout the dorsal and ventral sides of the embryo. At least 7 of those cilia were near the blastopore opening (Figure 4S), and none showed evidence for axonemal dyneins (Figures 4S–U), thus confirming the absence of motile cilia in the LRO of veiled chameleons.

## Morphological changes in the embryo temporally correlate with establishment of L-R asymmetry

Similar to veiled chameleons, avians and even-toed ungulates also lack motile cilia in their LROs (Gros et al., 2009). Instead, L-R asymmetry is established in these species when cells surrounding the node migrate in an asymmetric manner, such that the node becomes tilted (Wetzel, 1929; Cui et al., 2009; Gros et al., 2009). In avians, the

asymmetric morphology of the node is well established (Wetzel, 1929), but the asymmetric cell migration was revealed more recently through live imaging (Cui et al., 2009; Gros et al., 2009). Therefore, we evaluated chameleon embryonic development *via* live imaging to detect differences between the left and right sides in the establishment of L-R asymmetry. Veiled chameleons do not have a primitive streak or a distinct node, like avians or mammals, but have a blastopore slit instead (Stower et al., 2015). However, despite the morphological differences between chickens and chameleons, their patterns of gastrulation appear strikingly similar, with polonaise movements clearly visible in gastrulating chameleon embryos (Supplementary Video S2).

We successfully visualized the progression of L-R patterning through multiple timelapses of overlapping stages of development (Figure 5; Supplementary Videos S2–S4). Transverse optical sections (O.S.) revealed dynamic morphological changes in the embryos, which were consistent between different samples (Figure 5; Supplementary Videos S2–S4). As veiled chameleon embryos advance to stage 10 of development, we observed a subtle dorsal displacement of the left side of the embryo (Figures 5C', D'). This morphological change becomes very pronounced by stage 11, when the left side shifts much farther dorsally than the right side (Figures 5E', G' arrows). Subsequently, by the onset of somitogenesis, the right side of the veiled chameleon embryo moves dorsally to match the left side (Figures 5F', H' arrows). After that, both sides of the embryo appear to develop similarly from a dorsoventral morphological perspective. Notably, the earliest detectable morphological changes at stage 10 (Figures 5C, D, C', D') occur prior to the asymmetric *Nodal* expression (Figures 2D, K).

To circumvent the limitations of recording the development of embryos in culture with vital dyes, and to gain a better understanding and resolution of the processes that are taking place, we examined embryonic morphology in greater detail with RNA *in situ* markers and histological stains.

## Breaking L-R symmetry results from morphological changes during embryogenesis

To augment and further validate our live *ex ovo* imaging observations of the establishment of L-R asymmetry in veiled chameleon embryos, we performed expression analyses with classic genetic markers of morphological asymmetry in amniotes. We initially evaluated the expression of *Shh* (Figures 6A–G, D'–F', O), since it is recognized as one of the first genes to be expressed asymmetrically in chicken embryos (Levin et al., 1995). *Shh* expression first appears around stage 7 + in the prechordal plate of veiled chameleon embryos (Figures 6B–D, D'). Then as the midline develops, *Shh* expression becomes prominent in the floor plate and the notochordal plate (Figures 6D–G, D', E', F') similar to other vertebrates. Notably, *Shh* expression in the notochord and floor plate at all times and at all levels in the embryo is L-R symmetrical (Figures 6D', E', F').

In chicken embryos, *Fgf8* is expressed asymmetrically in the posterior perinodal region complementary to *Shh* and is believed to maintain asymmetric gene expression and repression on the right side of the embryo (Boettger et al., 1999; Monsoro-Burq and Levin, 2018). Likewise, *Fgf8* is expressed in the posterior of veiled



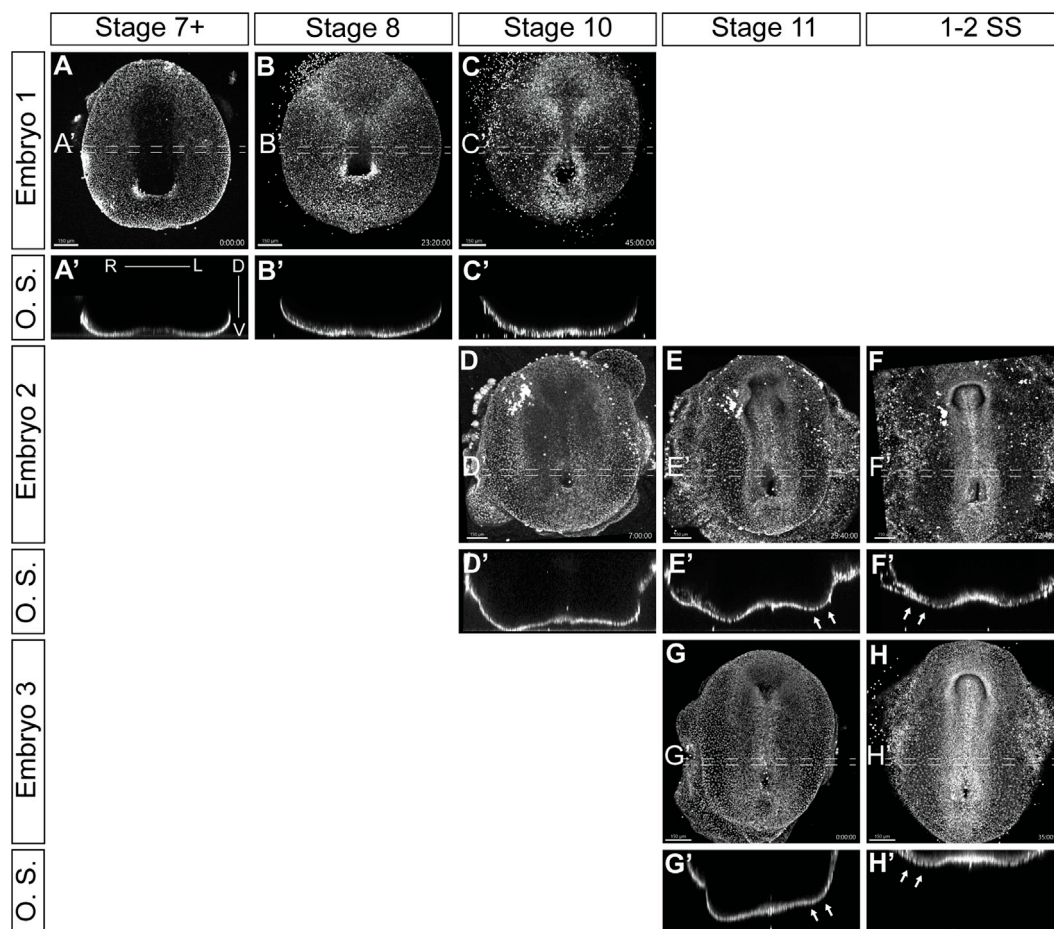


FIGURE 5

Video visualization of cellular migrations during gastrulation and left-right patterning. (A–H) Still images of developing embryos from [Supplementary videos S2–S4](#) show ventral view of embryos cultured with 5-SiR-Hoechst STED DNA dye to label nuclei. The punctate lines show the approximate region of the 40  $\mu\text{m}$  optical section. (A'–H') Transverse optical sections (O.S.) of embryos in (A–H), from the regions, indicated by punctate lines. Section orientation is as indicated in (A'). [Supplementary videos S2–S4](#) spanned different developmental stages, approximately assigned in the figure. White arrows in (E', F', G', H') show the areas of significant morphological changes in a developing embryo. Scale bars are in the bottom left corner of images and are 150  $\mu\text{m}$ .

chameleon embryos in a pattern complementary to *Shh* ([Supplementary Figures S6O–BB](#)). The onset of expression in chameleon is temporally similar to *Shh*, around stages 7–7+, becoming more pronounced in the posterior of the embryo throughout development ([Supplementary Figures S6O–BB, R', S', T', U'](#)). Similar to *Shh* expression, *Fgf8* is expressed symmetrically near the blastopore ([Supplementary Figures S6T', U'](#)).

When examining histological sections, we noted that the notochordal plate may also have L-R asymmetry in chameleon embryos ([Supplementary Figure S6S'](#) asterisk). We therefore used *Chordin* as an additional marker that labels both the floor plate and notochordal plate in veiled chameleon embryos in order to better examine notochordal plate morphology ([Figures 6H–N, K'–M'](#)). Its expression is strong at all timepoints examined and appears L-R symmetrical in both the floor plate and notochordal plate ([Figures 6K'–M'](#)).

Although *Shh*, *Fgf8* and *Chordin* are each expressed L-R symmetrically, as evident in transverse sections ([Figure 6; Supplementary Figure S6](#)), whole mount *in situ* hybridization staining revealed remarkable morphological L-R asymmetry of *Shh*

and *Chordin* ([Figure 6](#)) and, to a lesser degree *Fgf8* ([Supplementary Figure S6](#)), in the posterior region of the embryos, phenotypes most striking for the midline markers ([Figures 6D, E, O, L, M, P](#) arrowheads, [Supplementary Figures S6D, E, L, M, T, AA](#)). The asymmetry is most pronounced near the blastopore, with a deviation to the left ([Figures 6D, E, O, L, M, P](#) arrowheads, [Supplementary Figures S6D, E, L, M, T, AA](#)). This morphological asymmetry is transient and disappears with the onset of somitogenesis. It is important to emphasize that *Shh*, *Chordin* and *Fgf8* are not themselves expressed asymmetrically, but serve here as midline markers that highlight the morphological asymmetry ([Figure 6; Supplementary Figure S6](#)).

Transverse sections of stage 10, 11 and early somitogenesis embryos revealed the underlying morphological changes. The median hinge point of the forming neural tube is tilted to the left, instead of being centrally located (Arrows in [Figures 2, 3, 6; Supplementary Figure S6](#)). The notochordal plate likewise displays L-R morphological changes (Asterisk [Figure 6L'](#); [Supplementary Figure S6S'](#)). Lastly, transverse sections of stage 10–11 and early somite embryos reveal the presence of more mesoderm on the left side of the embryo, compared to the right



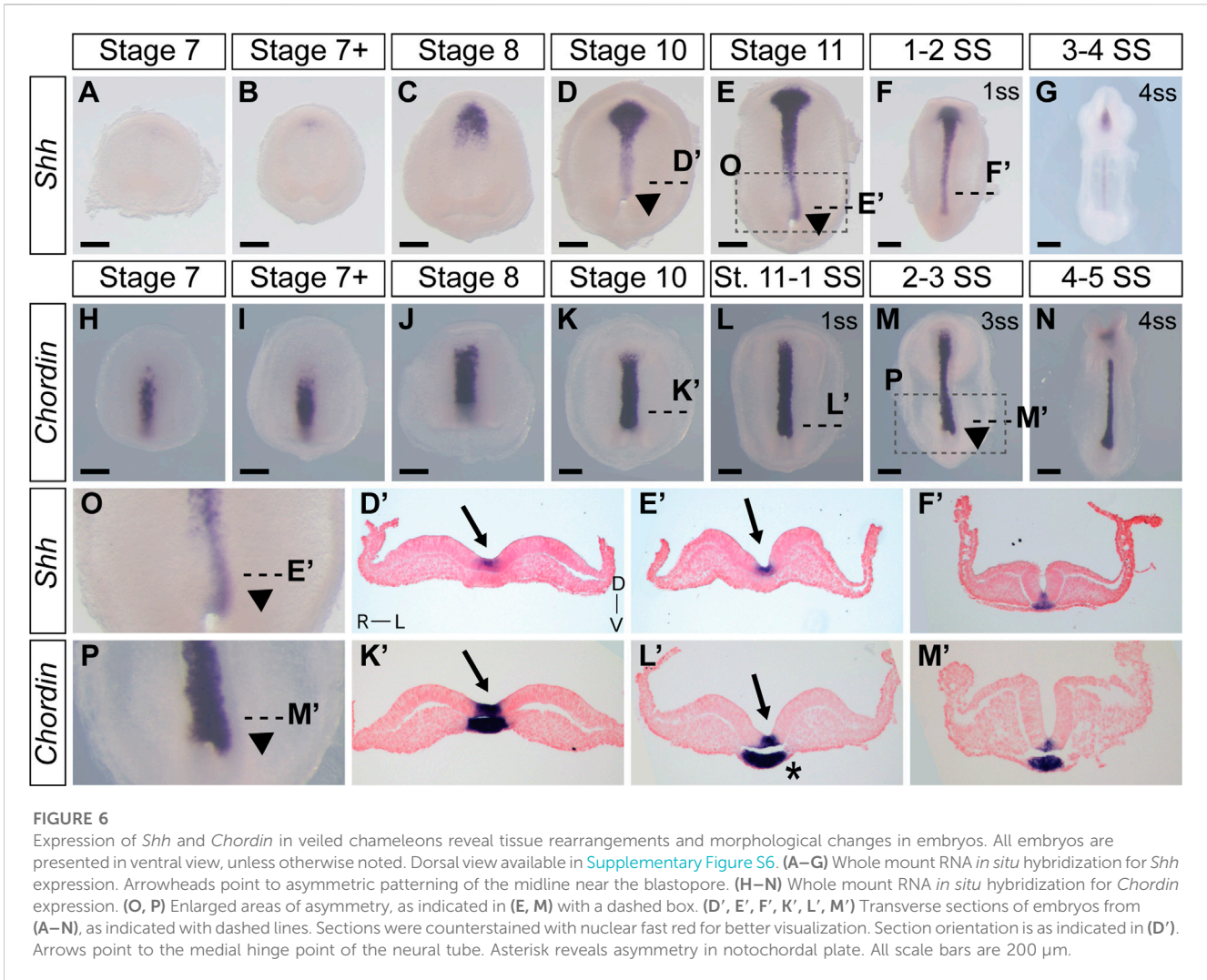


**FIGURE 6**

Expression of *Shh* and *Chordin* in veiled chameleons reveal tissue rearrangements and morphological changes in embryos. All embryos are presented in ventral view, unless otherwise noted. Dorsal view available in [Supplementary Figure S6](#). (A–G) Whole mount RNA *in situ* hybridization for *Shh* expression. Arrowheads point to asymmetric patterning of the midline near the blastopore. (H–N) Whole mount RNA *in situ* hybridization for *Chordin* expression. (O, P) Enlarged areas of asymmetry, as indicated in (E, M) with a dashed box. (D', E', F', K', L', M') Transverse sections of embryos from (A–N), as indicated with dashed lines. Sections were counterstained with nuclear fast red for better visualization. Section orientation is as indicated in (D'). Arrows point to the medial hinge point of the neural tube. Asterisk reveals asymmetry in notochordal plate. All scale bars are 200  $\mu\text{m}$ .

side (Most prominent in [Figures 2F', L', M', 3T''](#)). To confirm that these observations were not an artifact of dissected and processed embryos, we performed paraffin sectioning of additional embryos at stages 10 and 11 with all their embryonic and extraembryonic tissues intact ([Supplementary Figure S6CC, DD](#)). Hematoxylin and Eosin staining of transverse sections clearly reveal the displaced medial hinge point, and its asymmetric positioning in relation to the notochordal plate ([Supplementary Figure S6CC', DD'](#)).

Our observations from time lapse imaging and mRNA expression analyses corroboratively reveal that the onset of morphological changes in the embryo that lead to the establishment of L-R asymmetry, first occurs at stage 10, at a time when neither of the *Nodal* genes is expressed. Therefore, we propose that morphological changes in the embryo are central to the mechanism that triggers molecular L-R asymmetry in veiled chameleon embryos.

## Discussion

In this study we carried out a detailed developmental analysis of the breaking of L-R symmetry in veiled chameleon embryos and the mechanical and molecular mechanisms underpinning the process.

Non-avian reptiles do not have a conventional node, and instead use a blastopore slit for gastrulation, which likely preforms the functions of the LRO ([Stower and Bertocchini, 2017; Kajikawa et al., 2020](#)). Although motile cilia are central to the breaking of L-R symmetry in many vertebrate species, avians, turtles and geckos lack motile cilia in their LROs ([Kajikawa et al., 2020](#)). Similarly veiled chameleons also lack motile cilia in their blastopore, the presumed LRO, as L-R patterning becomes established. Thus, our study lends further support to the idea that the absence of motile cilia in the LRO is a synapomorphy of all reptiles.

While it was previously reported that *Nodal2* is the only *Nodal* ortholog conserved in reptiles ([Kajikawa et al., 2020](#)), we discovered that veiled chameleons possess two *Nodal* genes. We also found through genomic and phylogenetic comparisons that several other squamates also retained both *Nodal* genes in their genomes. In veiled chameleon, the expression of both orthologs is highly dynamic. *Nodal1* and *Nodal2* both appear to be involved in gastrulation and in L-R patterning but have distinct patterns of expression during gastrulation in different domains near the blastopore. Remarkably, the expression of both *Nodal* genes disappears abruptly at stage 8, coinciding with a strong burst of *Cer1* expression, symmetrical in the midline, together with *Lefty*

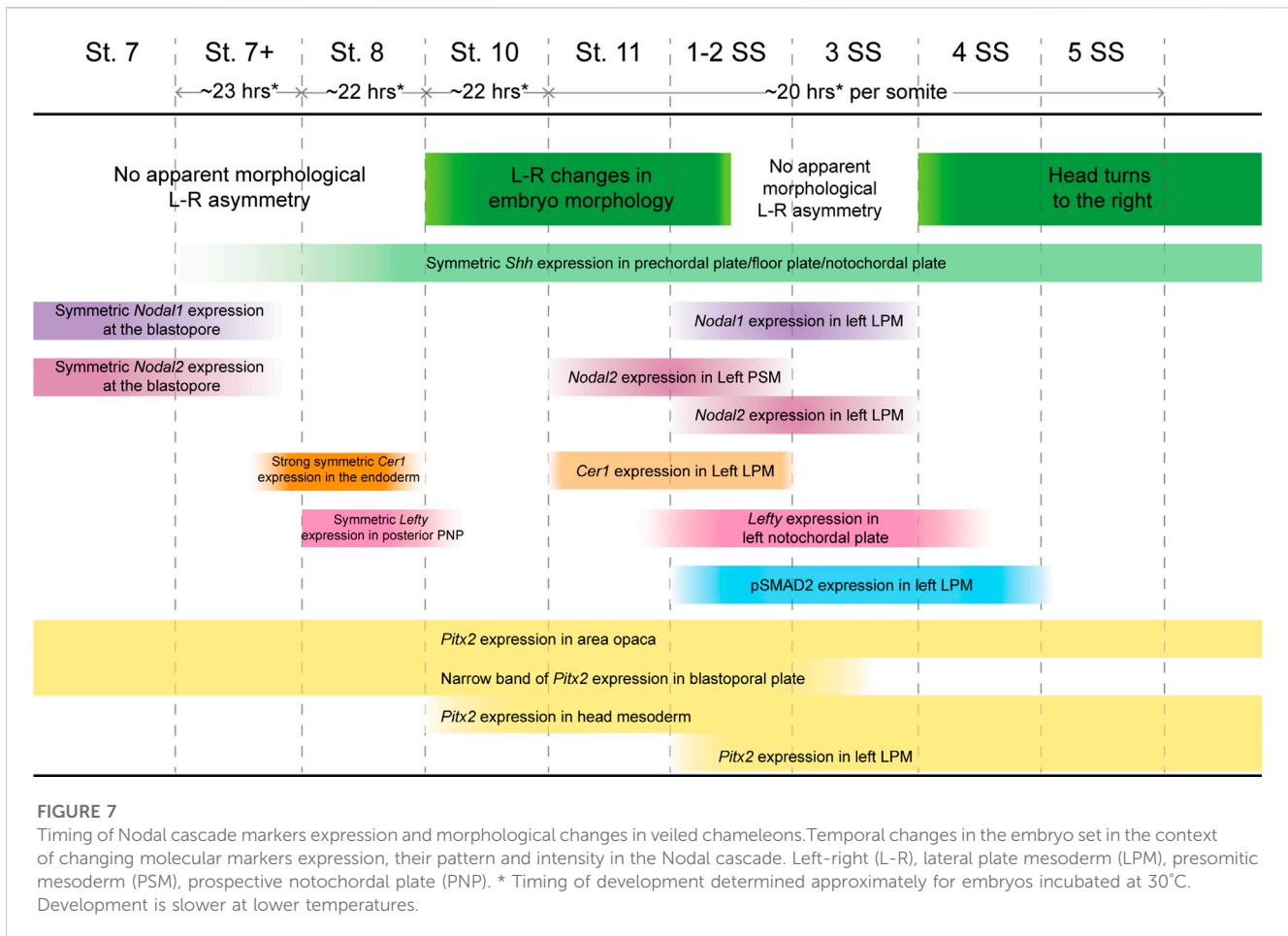


(Figure 7). The timing of these events implies that similar to observations in other species, *Cer1* and *Lefty* are indeed inhibitors of Nodal signaling in veiled chameleons. Furthermore, their re-activation subsequent to *Nodal2* expression in the left LPM is consistent with an activator-inhibitor model of gene regulation (Nakamura et al., 2006).

Typically, *Lefty* acts as a Nodal inhibitor in the left LPM. However, veiled chameleons lack *Lefty* expression in the left LPM. Thus, we speculate that the veiled chameleon *Lefty* gene may have been subject to significant regulatory changes. It is interesting to note however, that under circumstances of low *Nodal* expression, the presence of *Lefty* in the LPM may be dispensable in the establishment of L-R asymmetry (Rogers et al., 2017). *Cer1* is an alternative Nodal repressor. It belongs to the same family of genes as *Dand5*, a known *Nodal* repressor that has been lost from reptile genomes (Kajikawa et al., 2020). Based on its expression in the LPM, we believe that *Cer1* has replaced *Lefty* as the repressor of Nodal signaling in the left LPM of veiled chameleon embryos (Figure 7).

One of the most interesting findings that sets veiled chameleons apart from avians is the apparent mode for the initial break in L-R asymmetry. We originally observed these morphological changes *via* live imaging, which revealed dynamic changes on the left side of the embryo. The break in molecular L-R symmetry appears to be triggered by a morphological change in the embryo at stage 10. The posterior neural tube tilts such that the midline becomes

misaligned with the blastopore slit. We showed that these morphological changes are highlighted by *Shh* and *Chordin* midline expression. Interestingly, although not previously noted, similar molecular asymmetry involving different markers is also evident in turtle embryos (see Figure 4Q of Kajikawa et al., (2020); Figure 3G of Coolen et al. (2008)) (Coolen et al., 2008; Kajikawa et al., 2020). The morphological changes evident in veiled chameleons appear to be fundamentally different from avians and even-toed ungulates since there is no primitive streak and no node in this squamate reptile. In veiled chameleons, *Shh* and *Chordin* are expressed symmetrically within the floor plate and notochord, and provide a readout of morphological asymmetry, rather than drive the process. Furthermore, these morphological changes occur before any of the Nodal cascade markers are asymmetrically expressed (Figure 7).

We hypothesized that although neither *Nodal1* nor *Nodal2* is expressed at these stages, their proteins may be present and active. pSmad2 provides a read-out of active Nodal signaling, and, similar to *Nodal* gene expression, we could not detect pSmad2 until later stages, when it was limited to the left LPM. Thus, Nodal proteins are not the drivers of morphological asymmetries in veiled chameleon. Subsequently, asymmetric pSmad2 expression persists slightly longer than either of the *Nodal* transcripts, suggesting the retention of active Nodal protein at later stages in embryogenesis, after the transcript is downregulated.



Overall, it still remains to be determined what triggers these morphological changes and the initiation in the break in L-R symmetry in veiled chameleon. Several avenues for future study include exploration of the Marangoni flow (Matsushita et al., 2022) and its effects on collective cell movements, calcium signaling, establishment of planar cell polarity, as well as cellular chirality changes. Calcium has been shown to play a critical role in establishing L-R patterning in vertebrate embryos that utilize motile cilia, but its role is poorly understood in embryos that establish L-R patterning without the use of motile cilia in the LRO, like chicken embryos (Raya and Izpisua Belmonte, 2004; Yuan et al., 2015; Mizuno et al., 2020). Planar cell polarity, as well as chiral changes in cell shape are known to play important roles in L-R patterning in multiple organisms but remain unexplored in reptiles (Aw and Levin, 2009). The fact that veiled chameleon embryos are pre-gastrula at oviposition, coupled with their slow development (Figure 7), makes them an ideal model for exploring the earliest morphological and molecular mechanism underpinning the breaking of symmetry and evolution of L-R patterning in squamates.

## Methods

### Animal husbandry

All animal experiments were conducted in accordance with the Stowers Institute for Medical Research Institutional Animal Care and Use Committee approved protocol 2020-115. Veiled chameleon husbandry was performed in our Reptiles and Aquatics Facility as described previously (Diaz et al., 2015a; Diaz et al., 2015b; Diaz et al., 2017) following the protocols which are publicly available here: [dx.doi.org/10.17504/protocols.io.bzhsp36e](https://doi.org/10.17504/protocols.io.bzhsp36e).

### Data availability

All original data underlying this manuscript are available and can be accessed from the Stowers Original Data Repository at <http://www.stowers.org/research/publications/LIBPB-2378>

### Embryo collection and fixation

Veiled chameleon eggs were collected at oviposition in the Reptiles and Aquatics Facility at Stowers Institute for Medical Research. Eggs were incubated in deli cups with moist vermiculite at a constant temperature of 28°C. Late-stage embryos were harvested in 1X Phosphate Buffered Saline (PBS), decapitated, and fixed overnight in 4% Paraformaldehyde (PFA) in 1X PBS at 4°C. After washing in 1X PBS, organs were isolated and imaged. The lungs were isolated from fresh embryos intact and perfused with 4% PFA through the trachea, which inflated them. The trachea was tied off with a hair, and the entire lung was fixed overnight in 4% PFA at 4°C prior to imaging.

To collect early-stage embryos, eggs were incubated for 50–70 days post oviposition (dpo). The eggs were cleared of large particles and wiped with RNaseZap wipes (Invitrogen AM9786) to minimize RNase contamination. Clean eggs were candled to determine the position of the embryo under the leathery shell. We used fine scissors to cut a segment of the shell around the embryo and separate the embryo (attached to the shell) from the rest of the egg. The embryos were further separated from the shell and dissected out of the membranes in room temperature (RT) Tyrode's solution, made in DEPC-treated water. Subsequently the embryos were fixed overnight at 4°C in 4% PFA in DEPC 1X PBS, then dehydrated through an ascending methanol series into 100% methanol, and stored at –20°C for future analysis, including RNA *in situ* hybridization, immunofluorescent antibody staining and immunohistochemistry.

Stages of embryonic development were determined and reported in this paper after Dufaure and Hubert (1961) and Diaz et al. (2019), with slight adaptations (Supplementary Dataset S1).

To obtain kidney cells, a 95dpo embryo was dissected in sterile conditions. Both kidneys were extracted, minced with a scalpel, treated with 25% trypsin for 5 min, and then further dissociated into near-single cell suspension. The cells were plated into a 35 mm MatTek glass bottom culture dish (P35G-1.5-14-C) in the following culture media: DMEM/F-12 (Gibco 10565-018), 10% fetal bovine serum, 1X antibiotic antimycotic solution (Sigma Millipore A5955-100 ML) and 1 µg/mL gentamycin solution (VWR 97062-974) and allowed to attach overnight. The following morning the media was refreshed.

### Immunohistochemistry and immunofluorescent staining

Embryos were bleached in Dent's bleach for 2 h at room temperature after which they were rehydrated through a descending methanol series into PBS. Embryos were then thoroughly rinsed in PBS, incubated in blocking solution (PBS, 1% goat serum, 0.1% Tween-20) for 1 h at RT, followed by incubation with antibodies [MF-20, 1:25 (Developmental Studies Hybridoma Bank); pSMAD2, 1:500 (Cell Signaling Technology 3108S); and Arl13b 1:2000 (Proteintech 17711-1-AP)] in blocking solution overnight at 4°C. After washing thoroughly in blocking solution (3 × 20 min), the embryos were incubated in species-specific secondary antibodies for 2 h at RT. For immunofluorescence, secondary antibodies were conjugated to fluorophores, and DAPI was added to detect nuclei. We used an HRP-conjugated secondary antibody to detect for MF-20 staining. To remove excess antibody, embryos were washed 3 × 20 min in 1X PBS with 0.1% Triton-X. Embryos stained with pSMAD2, were washed overnight to decrease background staining. Fluorescent embryos were equilibrated through an ascending glycerol series and mounted in VECTASHIELD mounting medium (Vector Laboratories H-1200-10) between two coverslips to facilitate imaging of both the ventral and dorsal sides. MF-20 antibody labeling was developed using the DAB substrate kit for peroxidase staining (Vector Labs SK-4100).

Kidney cells were plated on 35 mm MatTek glass bottom culture dishes (P35G-1.5-14-C), and then fixed after live imaging, in 2% PFA for 20 min, and the antibody staining, and subsequent imaging proceeded in the dish.

## Imaging and image processing

Brightfield images of wholemount embryos were taken on a Leica MZ9.5 dissecting microscope, with a Leica DFC550 camera. Manual Z-stacks were taken of each embryo, and in-focus projections were generated using Helicon Focus 5.3 software. For larger embryos and organs, manual Z-stacks were coupled with manual tiling. In-focus tiles were then stitched using Photoshop.

Brightfield images of sectioned embryos post RNA *in situ* hybridization were acquired using a Lumenera Infinity3-3URC color CCD (2.8 MP) camera, running Micro-Manager ver. 1.4 (Edelstein et al., 2014) acquisition software on a Zeiss Axioplan 2i.e., upright microscope with HAL100 (100 W halogen) illumination.

Brightfield images of sectioned embryos stained with Hematoxylin and Eosin (H&E) were acquired with a Hamamatsu Flash 4.0 sCMOS camera on an Olympus VS.120 Whole Slide Scanner with 100 Slide Loader. Samples were illuminated by an UCB Transmission Lamp. The system was equipped with a neutral density filter for transmitted light. H&E samples were imaged with an UPLSAPO  $\times 20$  objective, NA 0.75 and illuminated with an UCB Transmission Lamp.

Fluorescent images of pSMAD2 stained embryos were obtained on a Zeiss LSM-700 laser scanning confocal microscope including a fully motorized upright Axio Imager. Z2 base, FixGate main beam splitter, automatic pinhole, continuously variable secondary dichroic beam splitter (VSD) to separate emission between 2 photomultipliers (PMT) with individual emission filters. Images were acquired with 405 nm (5 mW) and 488 nm (10 mW) excitation lasers with short pass 490 nm, band pass 490–555 nm emission filters and a Zeiss Fluor  $\times 5$  objective lens, N.A. 0.25. Gain was set to 588 for 405, 720 for 488.

Fluorescent images of Arl13b stained cells were acquired with a Zeiss LSM-700 laser scanning confocal microscope including a fully motorized upright Axio Imager. Z2 base, FixGate main beam splitter, automatic pinhole, continuously variable secondary dichroic beam splitter (VSD) to separate emission between two photomultipliers (PMT) with individual emission filters. Images were acquired with 405 nm (5 mW), 488 nm (10 mW), and 555 nm (10 mW) excitation lasers with short pass 490 nm, band pass 490–555 nm and band pass 505–600 nm emission filters and a Zeiss Plan-Apochromat  $\times 20$  objective lens, N.A. 0.8. Gain was set to 596 for 405, 559 for 488 and 544 for 555.

ImageJ was used to create maximum projections of imaged embryos and cells, and Photoshop and Illustrator were used to adjust brightness of fluorescent images, and further process them for the manuscript figures. When images were rotated for a display in anterior-posterior direction, missing background color at the edges of the images was filled in with Photoshop.

## Image normalization and fluorescence intensity measurement

pSMAD2 immunofluorescence images were normalized to DAPI as follows. In NIH ImageJ (Schneider et al., 2012), Z-stack images were sum projected, background subtracted, and subjected to a Gaussian blur of radius 2. From these images, a pixel-by-pixel ratio image of immunofluorescence to DAPI was calculated. The background region outside the embryo was cropped from the ratio image using a mask generated by performing an intensity threshold on the DAPI channel, with “fill holes” enabled. To quantify relative pSMAD2 staining across the embryo, normalized intensity profiles were generated from ratio images from line regions of interest (ROI) of width 200 pixels. A custom image analysis macro and instructions are available at Stowers Original Data Repository.

## RNA collection and cDNA synthesis

33 embryos from a single clutch, ranging from stage 7 of development to 8 somites were collected as described above. Embryos were pooled, and frozen at  $-80^{\circ}\text{C}$  with minimal liquid, until further processing. RNA was extracted using QIAGEN RNeasy Plus Mini Kit (74134), and purified RNA was submitted to Cold Spring Harbor for sequencing.

We used SuperScript III First-Strand Synthesis System for RT-PCR (Invitrogen 18080-051) for cDNA synthesis, utilizing 100 ng of RNA per reaction. We carried out both Oligo (dT) and randomer hexamers reactions. The two reactions were mixed, and that cocktail was used to clone gene fragments for RNA *in situ* hybridization probes (Supplementary Dataset S2).

## Transcriptome

RNA libraries were sequenced using the PacBio Sequel-II system at Cold Spring Harbor. Raw subread bam files were then used for consensus (CCS) generation, primer removal, demultiplexing, refining, and clustering using PacBio's established IsoSeq v3 pipeline (version 3.2.2). These clustered reads were then polished to generate a fasta file containing only high-quality isoforms with predicted accuracies  $\geq 0.99$ .

To generate a final set of non-redundant transcripts for gene discovery and annotation, the IsoSeq high-quality isoforms were run through Cogent (version v6.0.0) following the recommended protocol when no reference genome assembly is available. Cogent was used to partition input sequences into gene families based on k-mer similarity (using a k-mer size of 30) and reconstruct the coding region sequence for each gene family. The Iso-Seq high-quality isoform sequences were then aligned with minimap2 to a reference made from the reconstructed coding region sequences. From this alignment, cDNA Cupcake (version 10.0.1) was used to filter away isoforms with low counts of aligned full-length reads and isoforms with degraded 5' exons. Gene annotations were then assigned to each gene family coding region sequence using blastn megablast (BLAST 2.10.1+) with an e-value cutoff of



0.1 against the blast nt database and taking the single best blast hit.

The transcriptome shotgun assembly data were submitted to the NIH Sequence Read Archive (SRA: SRR22257482) and deposited at DDBJ/EMBL/GenBank and are available under the accession code GKDP00000000.

## Molecular phylogenetic analysis

We used known orthologous sequences of *Nodal1* and *Nodal2* genes to identify corresponding transcripts in the veiled chameleon transcriptome. We used open reading frames present in the transcripts as the presumed peptide sequences for veiled chameleon *Nodal1/2* proteins. The species and exact protein sequences selected for phylogenetic analysis were from Kajikawa et al. (2020). Protein sequences were retrieved from <https://www.uniprot.org/> (Consortium, 2020) and <https://www.ncbi.nlm.nih.gov/> (Sayers et al., 2022). We used the <https://ngphylogeny.fr/> web interface for all steps required to generate the phylogenetic tree (Lemoine et al., 2019). The multiple alignment was performed using MAFT with “linsi” option selected (Katoh and Standley, 2013). TrimAI was then used for alignment curation, with 0 gap threshold (Capella-Gutierrez et al., 2009). We used FastTree for tree inference with 1,000 bootstrap replicates (Price et al., 2009; Price et al., 2010; Lemoine et al., 2018). The resultant tree was displayed, managed and annotated using The Interactive Tree of Life web interface (<https://itol.embl.de/>) (Letunic and Bork, 2019). Branch lengths (mutations per site) are represented by numerical values.

## RNA *in situ* hybridization probes

PacBio mRNA sequencing results, as well as published transcriptome results (Pinto et al., 2019) were used to design probes of 350–800 bp in length (Supplementary Dataset S2). Fragments were amplified from cDNA and cloned into pCRII-TOPO (*Pitx2*, *FoxJ1*, *Dnah11*, *Lefty*), pCR-Blunt II-TOPO (*Nodal2*, *Cer1*, *Chordin*) or pGEM-T Easy (*Nodal1*). *Shh* and *Egf8* *in situ* plasmids were previously published (Diaz and Trainor, 2015).

## RNA *in situ* hybridization

RNA *in situ* hybridization was performed using the following protocol. Day1: Embryos were rehydrated through a descending methanol series from 100% methanol to PBT (PBS + 0.1% Tween-20), followed by further washes in PBT (2 × 5 min). The embryos were then incubated in 10 µg/mL Proteinase K in PBT for 7 min at RT, without rocking, followed by refixation in 4% PFA + 0.1% glutaraldehyde for 20 min. After washing in PBT (2 × 5 min), the embryos were incubated in 50/50 PBT/Prehybridization mix (50% formamide, 5XSSC pH 4.5, 2% SDS, 2% Blocking Reagent, 250 µg/mL torula RNA, 100 µg/mL heparin) for 5–10 min, followed by

prewarmed (68–70°C) prehybridization mix for 10 min at 68–70°C, then 1 h prehybridization mix at 68–70°C and finally prehybridization mix plus digoxigenin-labeled riboprobes (~1 µg/mL) overnight at 68–70°C.

The next day, embryos were rinsed in Solution X (50% formamide, 2X SSC pH 4.5, 1% SDS) at 68–70°C, followed by 4 × 30 min washes in Solution X at 68–70°C, then prewarmed solution X/MABT (1X MAB—Maleic acid, 0.1% Tween-20) 50/50 for 5–10 min. Embryos were then moved to RT, rinsed 3 × 5 min in MABT, followed by 2 × 30 min washes in MABT. The embryos were then incubated in 2% Blocking reagent (BR) in MABT for 1 h, followed by 20% Lamb Serum, 2% BR/MABT for 1–2 h, and then overnight in 20% Lamb Serum, 2% BR/MABT plus anti DIG-AP antibody (1:2000).

The next day, embryos were washed 3 × 5 min MABT, followed by 7 × 45 min MABT, 4 × 10 min in NTMT (100 mM NaCl, 100 mM Tris pH 9.5, 5 mM MgCl<sub>2</sub>, 1% Tween-20, 2 mM levamisole) and then finally NTMT + BCIP/NBT—at RT 1–2 h before continuing overnight in NTMT + BCIP/NBT at 4°C.

Color development continued at RT until the desired darkness of the substrate had been obtained. The total development time is typically 24–72 h, depending on the probe and NTMT + BCIP/NBT solution needs to be changed regularly. The color reaction was stopped with incubation in PBS and then embryos were stored long-term in 4% PFA at 4°C.

## Histological stains

After the whole mount embryos were imaged post RNA *in situ* hybridization, they were processed in 30% sucrose in 1X PBS for 1–2 h at RT, or until embryos sunk to the bottom of the tube. Then the embryos were equilibrated into Tissue-Tek O.C.T. Compound (VWR #25608-930) and embedded for frozen sectioning. Embryos were sectioned transversely to be 10 µm on a Leica or NX70 Cryostar cryostat, postfixed, stained with nuclear fast red for improved visualization of tissue morphology, dehydrated in ethanol and xylene series, and cover slipped for imaging and long-term storage.

To best determine morphological features in embryos, embryos were dissected as described, fixed overnight and dehydrated in ascending ethanol series into 70% ethanol. Embryos were embedded in paraffin and sectioned transversely to be 5 µm. Embryos were subsequently stained with H&E using standard techniques, dehydrated in ethanol and xylene series, and cover slipped for imaging and long-term storage.

## SEM and TEM imaging

For SEM imaging embryos were fixed in 4% PFA in 1X PBS and processed for SEM as previously described in Jongbloed et al. (1999) using tannic acid, osmium tetroxide, thiocarbohydrazide and osmium tetroxide (TOTO) to enhance conductivity before dehydration through a graded series of ethanol, followed by drying in a Tousimis Samdri 795 critical point dryer. Dried

samples were then mounted on stubs, coated with 4 nm gold palladium in a Leica ACE600 coater and imaged in a Zeiss Merlin SEM at 20 kV with SE2 detector.

For TEM analysis, embryos were prefixed with 2.5% paraformaldehyde and 2% glutaraldehyde in 50 mM sodium cacodylate containing 1% sucrose (pH 7.4). The samples were post fixed in 2% OsO<sub>4</sub>. After dehydration through a graded ethanol series, samples were infiltrated and embedded in Epon resin (EMS, Fort Washington, PA). Ultrathin (60–80 nm) sections were cut with a diamond knife and collected on single-slot copper grids. Grids were post-stained with 2% uranyl acetate and 1% lead citrate. Images were acquired on a FEI transmission electron microscope (Tecnai Bio-TWIN12, FEI) at 80 kV.

## Live imaging

Kidney cells, cultured in 35 mm MatTek glass bottom culture dish (P35G-1.5-14-C) as described above, were imaged with a Nikon Achromat TIRF ×60 objective with N.A. 1.49 with an Orca Flash 4.0 sCMOS at 100 fps at full resolution on a Nikon Eclipse Ti microscope equipped with a Yokagawa CSU W1 10,000 rpm Spinning Disk head with 50 μm pinholes. Samples were illuminated with transmitted white light LED light source. Fluorescent 2 μm beads (Polysciences Fluoresbrite<sup>®</sup> YG Microspheres 2.00 μm 18338-5) were added for better movement visualization.

Live embryos were dissected as described above and transferred to culture media containing DMEM/F-12 [Gibco 10565-018], 10% fetal bovine serum, 15% chick embryo extract (Bronner-Fraser et al., 2008), 1X antibiotic antimycotic solution (Sigma Millipore A5955-100 ML) and 1 μg/mL gentamycin solution (VWR 97062-974)]. Embryos were incubated in media and 5-SiR-Hoechst STED DNA dye (Bucevicius et al., 2019) (1:100 dilution) for 2 h at 28°C, and then mounted in the same media into an uncoated 35 mm glass bottom MatTek dish No. 1.5 (P35G-1.5-10-C) for imaging. Timelapse data were acquired on a Zeiss LSM-780 laser scanning confocal microscope equipped with a PMT, using a Plan-Apochromat ×10 objective lens (N.A. 0.45). Z stacks were collected with 10 μm spacing. Images were taken every 20 min at 30°C to speed up development.

## Video processing

Timelapse data were processed in ImageJ as follows. Movies were corrected for intensity changes over time (due to increasing dye uptake) using the histogram matching method (Miura, 2020). Xy drift was corrected by applying the rigid body method for image registration to a max projected version of the timelapse and applying the resulting displacement and angle corrections to the full data set (using the stackregJ plugin available at Github.com/jayunruh/jayplugins and based upon Thevenaz et al. (1998)). The resulting timelapse data were then rotated in ImageJ using the standard “Rotate” command, such that the anterior-posterior axis was parallel to the vertical y-axis of the image.

Stacks were imported into Imaris software (Oxford Instruments) to generate final movies. Anterior views were generated using the “MIP” mode of Volume rendering and the “camera type” setting on “Orthogonal”, while cross sectional views were generated at indicated regions using the “Ortho Slicer” tool.

## Data availability statement

The transcriptome shotgun assembly data were submitted to the NIH Sequence Read Archive (SRA: SRR22257482) and deposited at DDBJ/EMBL/GenBank. All original data underlying this manuscript are available and can be accessed from the Stowers Original Data Repository at <http://www.stowers.org/research/publications/LIBPB-2378>.

## Ethics statement

The animal study was reviewed and approved by Stowers Institute for Medical Research Institutional Animal Care and Use Committee protocol 2020-115.

## Author contributions

NS, SS, AJP, FG, MM, and PAT designed and performed experiments, and analyzed and interpreted data. All authors contributed to writing the manuscript.

## Funding

This work was supported by an Emerging Model Organism grant from the Society for Developmental Biology (NS) and the Stowers Institute for Medical Research (PT).

## Acknowledgments

The authors thank members of the Trainor lab for their insights and discussions throughout the course of this project. We are indebted to Rick Kupronis, David Jewell, Alex Muensch, Nikki Inlow, Diana Baumann and Elizabeth Evans and the Reptile Facility for their care, husbandry and maintenance of our veiled chameleon colony. We would like to thank the support of the Stowers technology centers, particularly microscopy for the live imaging help, and Hannah Wilson and Nancy Thomas from histology for paraffin sections and histological stains, as well as the bioinformatics team for assembling a *de novo* transcriptome.

## Conflict of interest

The authors declare that the research was conducted in the absence of any commercial or financial relationships that could be construed as a potential conflict of interest.



## Publisher's note

All claims expressed in this article are solely those of the authors and do not necessarily represent those of their affiliated organizations, or those of the publisher, the editors and the reviewers. Any product that may be evaluated in this article, or claim that may be made by its manufacturer, is not guaranteed or endorsed by the publisher.

## Supplementary material

The Supplementary Material for this article can be found online at: <https://www.frontiersin.org/articles/10.3389/fcell.2023.1132166/full#supplementary-material>

## References

- Aw, S., and Levin, M. (2009). Is left-right asymmetry a form of planar cell polarity? *Development* 136, 355–366. doi:10.1242/dev.015974
- Belo, J. A., Silva, A. C., Borges, A. C., Filipe, M., Bento, M., Goncalves, L., et al. (2009). Generating asymmetries in the early vertebrate embryo: The role of the cerberus-like family. *Int. J. Dev. Biol.* 53, 1399–1407. doi:10.1387/ijdb.072297jb
- Blum, M., Feistel, K., Thumberger, T., and Schweickert, A. (2014). The evolution and conservation of left-right patterning mechanisms. *Development* 141, 1603–1613. doi:10.1242/dev.100560
- Blum, M., and Ott, T. (2018). Animal left-right asymmetry. *Curr. Biol. CB* 28, R301–R304. doi:10.1016/j.cub.2018.02.073
- Blum, M., Weber, T., Beyer, T., and Vick, P. (2009). Evolution of leftward flow. *Seminars Cell & Dev. Biol.* 20, 464–471. doi:10.1016/j.semcdb.2008.11.005
- Boettger, T., Wittler, L., and Kessel, M. (1999). FGF8 functions in the specification of the right body side of the chick. *Curr. Biol. CB* 9, 277–280. doi:10.1016/s0960-9822(99)80119-5
- Bronner-Fraser, M., and Garcia-Castro, M. (2008). "Avian embryology," in *Methods in cell Biology*. Editor Marianne Bronner-Fraser. 2nd Ed. (Massachusetts, United States: Academic Press), 75–96.
- Bucevicius, J., Keller-Findeisen, J., Gilat, T., Hell, S. W., and Lukinavicius, G. (2019). Rhodamine-Hoechst positional isomers for highly efficient staining of heterochromatin. *Chem. Sci.* 10, 1962–1970. doi:10.1039/c8sc05082a
- Capella-Gutierrez, S., Silla-Martinez, J. M., and Gabaldon, T. (2009). trimAl: a tool for automated alignment trimming in large-scale phylogenetic analyses. *Bioinformatics* 25, 1972–1973. doi:10.1093/bioinformatics/btp348
- Chen, J., Knowles, H. J., Hebert, J. L., and Hackett, B. P. (1998). Mutation of the mouse hepatocyte nuclear factor/forkhead homologue 4 gene results in an absence of cilia and random left-right asymmetry. *J. Clin. Investigation* 102, 1077–1082. doi:10.1172/JCI4786
- Consortium, T. U. (2020). UniProt: The universal protein knowledgebase in 2021. *Nucleic Acids Res.* 49, D480–D489.
- Coolen, M., Nicolle, D., Plouhinec, J. L., Gombault, A., Sauka-Spengler, T., Menuet, A., et al. (2008). Molecular characterization of the gastrula in the turtle *Emys orbicularis*: An evolutionary perspective on gastrulation. *PLoS One* 3, e2676. doi:10.1371/journal.pone.0002676
- Cui, C., Little, C. D., and Rongish, B. (2009). Rotation of organizer tissue contributes to left-right asymmetry. *Anat. Rec.* 292, 557–561. doi:10.1002/ar.20872
- Diaz, R. E., Jr., Anderson, C. V., Baumann, D. P., Kupronis, R., Jewell, D., Piraquive, C., et al. (2015). Captive care, raising, and breeding of the veiled chameleon (*Chamaeleo calytratus*). *Cold Spring Harb. Protoc.* 2015, 943–949. doi:10.1101/pdb.prot087718
- Diaz, R. E., Jr., Anderson, C. V., Baumann, D. P., Kupronis, R., Jewell, D., Piraquive, C., et al. (2015). The veiled chameleon (*Chamaeleo calytratus* dumeril and dumeril 1851): A model for studying reptile body plan development and evolution. *Cold Spring Harb. Protoc.* 2015, 889–894. doi:10.1101/pdb.emo087700
- Diaz, R. E., Jr., Bertocchini, F., and Trainor, P. A. (2017). Lifting the veil on reptile embryology: The veiled chameleon (*Chamaeleo calytratus*) as a model system to study reptilian development. *Methods Mol. Biol.* 1650, 269–284. doi:10.1007/978-1-4939-7216-6\_18
- Diaz, R. E., Jr., Shylo, N. A., Roellig, D., Bronner, M., and Trainor, P. A. (2019). Filling in the phylogenetic gaps: Induction, migration, and differentiation of neural crest cells in a squamate reptile, the veiled chameleon (*Chamaeleo calytratus*). *Dev. Dyn. official Publ. Am. Assoc. Anatomists* 248, 709–727. doi:10.1002/dvdy.38
- Diaz, R. E., Jr., and Trainor, P. A. (2015). Hand/foot splitting and the 're-evolution' of mesopodial skeletal elements during the evolution and radiation of chameleons. *BMC Evol. Biol.* 15, 184. doi:10.1186/s12862-015-0464-4
- Dufaure, J., and Hubert, J. (1961). Table de développement du lézard vivipare-Lacerta (*Zootoca*) vivipara Jacquin. *Archives D Anatomie Microsc. De Morphol. Exp.* 50, 309–327.
- Edelstein, A. D., Tsuchida, M. A., Amodaj, N., Pinkard, H., Vale, R. D., and Stuurman, N. (2014). Advanced methods of microscope control using µManager software. *J. Biol. Methods* 1, e10. doi:10.14440/jbm.2014.36
- Gilland, E., and Burke, A. (2004). in *Gastrulation: From cells to embryo*. Editor C. D. Stern (New York, United States: Cold Spring Harbor Laboratory Press), 205–217.
- Gros, J., Feistel, K., Viebahn, C., Blum, M., and Tabin, C. J. (2009). Cell movements at Hensen's node establish left/right asymmetric gene expression in the chick. *Science* 324, 941–944. doi:10.1126/science.1172478
- Hashimoto, H., Uji, S., Kurokawa, T., Washio, Y., and Suzuki, T. (2007). Flounder and fugu have a single lefty gene that covers the functions of lefty1 and lefty2 of zebrafish during L-R patterning. *Gene* 387, 126–132. doi:10.1016/j.gene.2006.08.025
- Hoyle, C., Brown, N. A., and Wolpert, L. (1992). Development of left/right handedness in the chick heart. *Development* 115, 1071–1078. doi:10.1242/dev.115.4.1071
- Jongebloed, W. L., Stokroos, I., Van der Want, J. J., and Kalicharan, D. (1999). Non-coating fixation techniques or redundancy of conductive coating, low kV FE-SEM operation and combined SEM/TEM of biological tissues. *J. Microsc.* 193, 158–170. doi:10.1046/j.1365-2818.1999.00430.x
- Kajikawa, E., Horo, U., Ide, T., Mizuno, K., Minegishi, K., Hara, Y., et al. (2020). Nodal paralogs underlie distinct mechanisms for visceral left-right asymmetry in reptiles and mammals. *Nat. Ecol. Evol.* 4, 261–269. doi:10.1038/s41559-019-1072-2
- Katoh, K., and Standley, D. M. (2013). MAFFT multiple sequence alignment software version 7: Improvements in performance and usability. *Mol. Biol. Evol.* 30, 772–780. doi:10.1093/molbev/mst010
- Klaver, C. J. J. (1973). Lung-anatomy: Aid in chameleon-taxonomy. *Beaufortia Ser. Misc. Publ.* 20, 155–177.
- Lemoine, F., Correia, D., Lefort, V., Doppelt-Azeroual, O., Mareuil, F., Cohen-Boulakia, S., et al. (2019). NGPhylogeny fr: New generation phylogenetic services for non-specialists. *Nucleic Acids Res.* 47, W260–W265. doi:10.1093/nar/gkz303
- Lemoine, F., Domelevo Entfellner, J. B., Wilkinson, E., Correia, D., Davila Felipe, M., De Oliveira, T., et al. (2018). Renewing Felsenstein's phylogenetic bootstrap in the era of big data. *Nature* 556, 452–456. doi:10.1038/s41586-018-0043-0
- Letunic, I., and Bork, P. (2019). Interactive tree of Life (iTOL) v4: Recent updates and new developments. *Nucleic Acids Res.* 47, W256–W259. doi:10.1093/nar/gkz239
- Levin, M., Johnson, R. L., Stern, C. D., Kuehn, M., and Tabin, C. (1995). A molecular pathway determining left-right asymmetry in chick embryogenesis. *Cell* 82, 803–814. doi:10.1016/0092-8674(95)90477-8
- Levin, M., Pagan, S., Roberts, D. J., Cooke, J., Kuehn, M. R., and Tabin, C. J. (1997). Left/right patterning signals and the independent regulation of different aspects of situs in the chick embryo. *Dev. Biol.* 189, 57–67. doi:10.1006/dbio.1997.8662
- Lin, C. R., Kiousi, C., O'Connell, S., Briata, P., Szeto, D., Liu, F., et al. (1999). Pitx2 regulates lung asymmetry, cardiac positioning and pituitary and tooth morphogenesis. *Nature* 401, 279–282. doi:10.1038/45803
- Maerker, M., Getwan, M., Dowdle, M. E., McSheene, J. C., Gonzalez, V., Pelliccia, J. L., et al. (2021). Bicc1 and Dicer regulate left-right patterning through post-transcriptional

- control of the Nodal inhibitor Dand5. *Nat. Commun.* 12, 5482. doi:10.1038/s41467-021-25464-z
- Marra, A. N., Li, Y., and Wingert, R. A. (2016). Antennas of organ morphogenesis: The roles of cilia in vertebrate kidney development. *Genesis* 54, 457–469. doi:10.1002/dvg.22957
- Matsushita, K., Hashimura, H., Kuwayama, H., and Fujimoto, K. (2022). Collective cell movement under cell-scale tension gradient at tissue interface. *J. Phys. Soc. Jpn.* 91, 054802. doi:10.7566/jpsj.91.054802
- Meno, C., Shimono, A., Saijoh, Y., Yashiro, K., Mochida, K., OhiShi, S., et al. (1998). *lefty-1* is required for left-right determination as a regulator of *lefty-2* and *nodal*. *Cell* 94, 287–297. doi:10.1016/s0092-8674(00)81472-5
- Miura, K. (2020). Bleach correction ImageJ plugin for compensating the photobleaching of time-lapse sequences. *F1000Research* 9, 1494. doi:10.12688/f1000research.27171.1
- Mizuno, K., Shiozawa, K., Katoh, T. A., Minegishi, K., Ide, T., Ikawa, Y., et al. (2020). Role of Ca(2+) transients at the node of the mouse embryo in breaking of left-right symmetry. *Sci. Adv.* 6, eaba1195. doi:10.1126/sciadv.aba1195
- Monsoro-Burq, A. H., and Levin, M. (2018). Avian models and the study of invariant asymmetry: How the chicken and the egg taught us to tell right from left. *Int. J. Dev. Biol.* 62, 63–77. doi:10.1387/ijdb.180047ml
- Nakamura, T., Mine, N., Nakaguchi, E., Mochizuki, A., Yamamoto, M., Yashiro, K., et al. (2006). Generation of robust left-right asymmetry in the mouse embryo requires a self-enhancement and lateral-inhibition system. *Dev. Cell* 11, 495–504. doi:10.1016/j.devcel.2006.08.002
- Opazo, J. C., Kuraku, S., Zavala, K., Toloza-Villalobos, J., and Hoffmann, F. G. (2019). Evolution of nodal and nodal-related genes and the putative composition of the heterodimers that trigger the nodal pathway in vertebrates. *Evol. Dev.* 21, 205–217. doi:10.1111/ede.12292
- Pinto, B. J., Card, D. C., Castoe, T. A., Diaz, R. E., Nielsen, S. V., Trainor, P. A., et al. (2019). The transcriptome of the veiled chameleon (*Chamaeleo calyptratus*): A resource for studying the evolution and development of vertebrates. *Dev. Dyn.* 248, 702–708. doi:10.1002/dvdy.20
- Price, M. N., Dehal, P. S., and Arkin, A. P. (2009). FastTree: Computing large minimum evolution trees with profiles instead of a distance matrix. *Mol. Biol. Evol.* 26, 1641–1650. doi:10.1093/molbev/msp077
- Price, M. N., Dehal, P. S., and Arkin, A. P. (2010). FastTree 2—approximately maximum-likelihood trees for large alignments. *PLoS One* 5, e9490. doi:10.1371/journal.pone.0009490
- Raya, A., and Izpisua Belmonte, J. C. (2004). Unveiling the establishment of left-right asymmetry in the chick embryo. *Mech. Dev.* 121, 1043–1054. doi:10.1016/j.mod.2004.05.005
- Rodriguez Esteban, C., Capdevila, J., Economides, A. N., Pascual, J., Ortiz, A., and Izpisua Belmonte, J. C. (1999). The novel Cer-like protein Caronte mediates the establishment of embryonic left-right asymmetry. *Nature* 401, 243–251. doi:10.1038/45738
- Rogers, K. W., Lord, N. D., Gagnon, J. A., Pauli, A., Zimmerman, S., Aksel, D. C., et al. (2017). Nodal patterning without Lefty inhibitory feedback is functional but fragile. *eLife* 6, e28785. doi:10.7554/eLife.28785
- Ryan, A. K., Blumberg, B., Rodriguez-Esteban, C., Yonei-Tamura, S., Tamura, K., Tsukui, T., et al. (1998). Pitx2 determines left-right asymmetry of internal organs in vertebrates. *Nature* 394, 545–551. doi:10.1038/29004
- Sayers, E. W., Bolton, E. E., Brister, J. R., Canese, K., Chan, J., Comeau, D. C., et al. (2022). Database resources of the national center for biotechnology information. *Nucleic Acids Res.* 50, D20–D26. doi:10.1093/nar/gkab112
- Schneider, C. A., Rasband, W. S., and Eliceiri, K. W. (2012). NIH image to ImageJ: 25 years of image analysis. *Nat. Methods* 9, 671–675. doi:10.1038/nmeth.2089
- Stower, M. J., and Bertocchini, F. (2017). The evolution of amniote gastrulation: The blastopore-primitive streak transition. *Wiley Interdiscip. Rev. Dev. Biol.* 6, 262. doi:10.1002/wdev.262
- Stower, M. J., Diaz, R. E., Fernandez, L. C., Crother, M. W., Crother, B., Marco, A., et al. (2015). Bi-modal strategy of gastrulation in reptiles. *Developmental* 244, 1144–1157. doi:10.1002/dvdy.24300
- Supp, D. M., Witte, D. P., Potter, S. S., and Brueckner, M. (1997). Mutation of an axonemal dynein affects left-right asymmetry in *inversus viscerum* mice. *Nature* 389, 963–966. doi:10.1038/40140
- Tavares, A. T., Andrade, S., Silva, A. C., and Belo, J. A. (2007). Cerberus is a feedback inhibitor of Nodal asymmetric signaling in the chick embryo. *Development* 134, 2051–2060. doi:10.1242/dev.000901
- Thevenaz, P., Ruttimann, U. E., and Unser, M. (1998). A pyramid approach to subpixel registration based on intensity. *IEEE Trans. Image Process.* 7, 27–41. doi:10.1109/83.650848
- Waddington, C. H. (1937). The dependence of head curvature on the development of the heart in the chick embryo. *J. Exp. Biol.* 14, 229–231. doi:10.1242/jeb.14.2.229
- Watanabe, H., Schmidt, H. A., Kuhn, A., Hoger, S. K., Kocagöz, Y., Laumann-Lipp, N., et al. (2014). Nodal signalling determines biradial asymmetry in Hydra. *Nature* 515, 112–115. doi:10.1038/nature13666
- Wetzel, R. (1929). *Untersuchungen am Hühnchen*. Heidelberg, Germany: Springer, 188–321.
- Yoshioka, H., Meno, C., Koshiba, K., Sugihara, M., Itoh, H., Ishimaru, Y., et al. (1998). Pitx2, a bicoid-type homeobox gene, is involved in a lefty-signaling pathway in determination of left-right asymmetry. *Cell* 94, 299–305. doi:10.1016/s0092-8674(00)81473-7
- Yuan, S., Zhao, L., Brueckner, M., and Sun, Z. (2015). Intraciliary calcium oscillations initiate vertebrate left-right asymmetry. *Curr. Biol. CB* 25, 556–567. doi:10.1016/j.cub.2014.12.051